Investigations on the Droplet Impact onto a Spherical Surface with a High Density Ratio Multi-Relaxation Time Lattice-Boltzmann Model

Duo Zhang[1,2], K. Papadikis[1,*] and Sai Gu[3]

[1] *Xi'an Jiaotong-Liverpool University, No. 111 Ren'ai Road, Suzhou Dushu Lake Higher Education Town, Suzhou, China 215123.*
[2] *School of Engineering, University of Liverpool, Brownlow Hill, Liverpool, L69 7ZX, United Kingdom.*
[3] *School of Engineering, Cranfield University, Bedfordshire MK43 0AL, United Kingdom.*

Abstract. In the current study, a two-dimensional multi-relaxation time (MRT) lattice Boltzmann model which can tolerate high density ratios and low viscosity is employed to simulate the liquid droplet impact onto a curved target. The temporal variation of the film thickness at the north pole of the target surface is investigated. Three different temporal phases of the dynamics behavior, namely, the initial drop deformation phase, the inertia dominated phase and the viscosity dominated phase are reproduced and studied. The effect of the Reynolds number, Weber number and Galilei number on the film flow dynamics is investigated. In addition, the dynamic behavior of the droplet impact onto the side of the curved target is shown, and the effect of the contact angle, the Reynolds number and the Weber number are investigated.

1 Introduction

Many engineering process operations involve the droplet impingement onto solid surface, such as spray cooling, spray painting and coating, diesel and automotive injection, catalytic reaction process in fixed bed reactors and more recently in microfabrication and

---

*Corresponding author. *Email address:* `Konstantinos.Papadikis@xjtlu.edu.cn` (K. Papadikis)

microchannels. Therefore, understanding the fluid dynamics of droplet impaction onto solid surfaces is important for the design and improvement of the above industrial processes.

Rein [1] and Yarin [2] presented comprehensive reviews on the experimental and theoretical studies of the droplet impact dynamics onto the solid surface. Systematic studies have been carried out by Rioboo et al. [3]. Six possible outcomes of drop impact on a dry wall were revealed, namely deposition, prompt splash, corona splash, receding break-up, partial rebound and complete rebound. The influence of droplet size, impact velocity, droplet viscosity, surface tension of the droplet, the surface roughness amplitude and the surface wettability characteristics on the impingement outcomes have been investigated. Experimental and analytical investigations have been done extensively to study the time evolution of the spread factor and the correlation between the maximum spreading factor and Weber number, Reynolds number, Ohnesorge number [4–8]. The three non-dimensional parameters, Weber number (*We*), Reynolds number (*Re*) and the Ohnesorge number (*Oh*) are defined as

$$We = \frac{\rho_L D_0 U_0^2}{\sigma}, \tag{1.1}$$

$$Re = \frac{\rho_L D_0 U_0}{\mu_L} \tag{1.2}$$

$$Oh = \frac{\mu_L}{\sqrt{D_0 \sigma \rho_L}}, \tag{1.3}$$

where U_0 is the drop impaction speed, D_0 is diameter of the spherical drop prior to impact, μ_L is the liquid viscosity, σ is surface tension of the liquid drop, ρ_L is liquid density.

Most of the existing work has investigated the droplet impacting onto a flat surface. However, very limited research has been focused on the droplet impacting onto a spherical surface. Hung and Yao [9] have carried out experiments on the impaction of water droplets, the diameters of which are 110, 350 and 680 μm on cylindrical wires. The effect of droplet velocity and the wire sizes were varied parametrically to reveal the impaction characteristics. Hardalupas et al. [10] have conducted experiments on droplets of a water-ethanol-glycerol solution in the size and velocity ranges of $160 < D < 230$ μm and $6 < U < 13$ m/s respectively, impinging on the surface of a solid sphere with $0.8 - 1.3$ *mm* diameter. The impinged droplet formed a crown which was influenced by surface roughness, droplet kinematic and liquid properties. Bakshi et al. [11] have reported experiments and theory on the impact of a droplet onto a spherical target over a range of Reynolds numbers and target-to-drop size ratios. Three distinct temporal phases of the film dynamics were found, namely the initial drop deformation phase, the inertia dominated phase, and the viscosity dominated phase. The influence of the droplet Reynolds number and the target-to-drop size ratio on the dynamics of the film flow on the surface of the target were conducted.

Since experimental techniques are not adequate to deal with the complex measurement, numerical investigations have drawn increasing attention in simulating complex

multi-phase flow. Trapaga and Szekely [12] used a commercial code (FLOW-3D) that implements the "volume of fluid" (VOF) method to study the impact of molten particles in a thermal spray process. Bussmann et al. [13] studied the flow of a droplet impact on flat and inclined surfaces with a 3D VOF method. Pasandideh-Fard et al. [14] developed a three-dimensional model which is an extension of finite-difference, fixed-grid Eulerian model to simulated the impact of a 2*mm* diameter water droplet landing with low velocity (1*m/s*) on tubes ranging in diameter from 0.5 to 6.35 *mm*. Liu et al. [15] developed a fixed-grid, sharp interface method to simulate the droplet impact and spreading on surfaces of arbitrary shape with a level-set method. Ge and Fan [16] studied the process of collision between an evaporative droplet and a high-temperature particle in a riser reactor with a three-dimensional level-set method.

As a modern method, lattice Boltzmann method (LBM) has attracted considerable attention in simulating the droplet impingement on solid surfaces. There are several models developed for multi-phase and multi-component flows during the last twenty years. They are Shan and Chen's potential method [17], Swift et al.'s free energy method [18] and He et al.'s phase field method [19]. However, the density ratio is limited due to numerical instabilities. To overcome this difficulty, Inamuro et al. [20] proposed a model, based on the free energy method for multi-phase flows with large density ratio. Yan [21] reported a new numerical scheme for the lattice Boltzmann method which combines the existing model of Inamuro [20] and Briant [22] for calculating the liquid droplet behavior on partial wetting surface typically for the system of liquid-gas of large density ratio. However, Inamuro et al.'s model [20] involves solving a Poisson equation, which decreased the simplicity of the usual LBM. Lee and Liu [23] developed a stabilized scheme of discrete Boltzmann equation for multiphase flows with large density ratio based on the phase field method. The LBE method was applied to micron-scale drop impact on dry surfaces. However, at different steps, the discretization forms are different, which make the implementation quite complex and reduce the computational efficiency greatly. Alternative to the Bhatnagar-Gross-Krook (BGK) model, the multi-relaxation time (MRT) method [24–26], represent changes in the various physical collision processes by selecting different and separated time scales. The stability of the LBE can be significantly improved by MRT. Gupta and Kumar [27, 28] studied the droplet impingement on a flat solid surface with Shan-Chen model [17] at low density ratio. However, the Shan-Chen model adopted in the present study suffers from some limitations, such as low density ratios and it is unstable with a relaxation time τ less than 1 which restricts the maximum Reynolds number that can be achieved. Very few studies focus on the simulation of a droplet impact on a curved solid surface. Shen [29] adopted the two-dimensional lattice Boltzmann pseudo-potential method to simulate the droplets impacting on curved solid surfaces. However, the density ratio of liquid and gas is limited to unity.

In order to overcome the limitations of low density ratio and instability with a relaxation time τ less than 1, a two-dimensional multi-relaxation-time interaction-potential-based lattice Boltzmann model based on the improved forcing scheme which was reported by Li et al. [30] and Peng-Robinson (P-R) equation of state [31] is proposed in this

paper. The impaction of liquid droplet on a curved surface for the liquid-gas system with large density ratio and low kinematic viscosity of the fluid is simulated. The effect of the Reynolds number, Weber number, Galilei number and surface characteristics on the dynamic behavior of droplet and film flow dynamics on the target surface are investigated.

The rest of the paper is organized in four sections. In Section 2, the improved MRT pseudopotential LBM model is introduced, followed by numerical investigations on the droplet impact onto a spherical surface in Section 3. Finally, conclusions are presented in Section 4.

2 Numerical model

2.1 Incorporation of the force term

In the LBM model, the motion of a fluid is described by a set of discrete single-particle density distribution functions. According to the Guo et al. [32] forcing scheme, the particle distribution function with single relaxation time can be written as

$$f_\alpha(x+e_\alpha\delta t,t+\delta t)=f_\alpha(x,t)-\frac{1}{\tau}[f_\alpha(x,t)-f_\alpha^{eq}(x,t)]+F_\alpha, \tag{2.1}$$

where f_α is the particle distribution along the αth direction and f_α^{eq} is equilibrium distribution, δt is the time step, e_α is the particle velocity in the αth direction, and τ is the single relaxation time. F_α is the forcing term, Li et al. [30] proposed an improved version based on Guo et al. forcing scheme by using a modified velocity in the scheme, which leads to

$$F_\alpha=(1-\frac{1}{2\tau})w_\alpha\left[\frac{e_\alpha-v'}{c_s^2}+\frac{(e_\alpha\cdot v')}{c_s^4}e_\alpha\right]\cdot F. \tag{2.2}$$

The modified velocity v' is defined as $v'=v+\epsilon F/((\tau-0.5)\psi^2)$, where ψ is the effective mass and ϵ is a constant. $c_s=c/\sqrt{3}$ is the lattice sound speed, where $c=\delta x/\delta t$ is the ratio of lattice spacing δx and time step δt. The equilibrium distribution function $f_\alpha^{eq}(x,t)$ in Eq. (2.1) can be calculated as

$$f_\alpha^{eq}=\rho w_\alpha\left[1+\frac{e_\alpha\cdot v}{c_s^2}+\frac{(e_\alpha\cdot v)^2}{2c_s^4}-\frac{v}{2c_s^2}\right], \tag{2.3}$$

where w_α is the weighting factor. In this paper, the D2Q9 model will be adopted for 2D simulations. The discrete velocity and weighting factor for D2Q9 are given by

$$\left[\, e_0,e_1,e_2,e_3,e_4,e_5,e_6,e_7,e_8 \,\right]=\begin{bmatrix} 0 & 1 & 0 & -1 & 0 & 1 & -1 & -1 & 1 \\ 0 & 0 & 1 & 0 & -1 & 1 & 1 & -1 & -1 \end{bmatrix}, \tag{2.4}$$

$$w_\alpha=\begin{cases} 4/9, & \alpha=0; \\ 1/9, & \alpha=1,2,3,4; \\ 1/36, & \alpha=5,6,7,8. \end{cases} \tag{2.5}$$

The corresponding macroscopic density and velocity are calculated by

$$\rho(x,t) = \sum_{\alpha=0}^{N} f_\alpha(x,t), \tag{2.6}$$

$$\rho v(x,t) = \sum_{\alpha=0}^{N} e_\alpha f_\alpha(x,t) + \frac{F}{2}, \tag{2.7}$$

where N is the number of discrete particle velocities. $F = F_1 + F_2 + F_3$ is the total force on each particle, including fluid-fluid cohesion F_1, fluid-solid adhesion force F_2 and body force F_3.

2.2 Fluid-fluid cohesion

It is commonly accepted that the segregation of different phases is microscopically due to the long-range interaction force between the particles at site x and the particles at neighbor sites x' [17]. The interaction force is defined as:

$$F_1(x) = -\psi(x) \sum_{x'} G(x,x') \psi(x')(x' - x), \tag{2.8}$$

where $G(x,x')$ is Green's function and satisfies $G(x,x') = G(x',x)$. It reflects the intensity of the interparticle interaction and given by

$$G(x,x') = \begin{cases} g', & |x - x'| = 1, \\ g'/4, & |x - x'| = \sqrt{2}, \\ 0, & \text{otherwise}, \end{cases} \tag{2.9}$$

where g' is a constant equals to $1/9$ in the current work. In Eq. (2.8), $\psi(x)$ is the effective mass, which is a function of the local density and can be varied to reflect different fluid and fluid mixture behaviors, as represented by various equations. The equation of state (EOS) of the system is given by

$$p = c_s^2 \rho + \frac{c_0}{2} g[\psi(\rho)]^2, \tag{2.10}$$

thus the effective mass can be defined as:

$$\psi(\rho) = \sqrt{\frac{2(p - c_s^2 \rho)}{c_0 g}}, \tag{2.11}$$

where $g = g'/2$ is a constant and $c_0 = 6.0$ for the D2Q9, and p is the pressure. Five different EOS were compared by Yuan and Schaefer [31], and it was found that Peng-Robinson (P-R) EOS provided the maximum density ratio while maintaining small spurious currents

around the interface. Hence, the P-R EOS was adopted in our following multi-phase flow research, where the P-R EOS is expressed as:

$$p = \frac{\rho RT}{1-b\rho} - \frac{a\alpha(T)\rho^2}{1+2b\rho-b^2\rho^2}, \tag{2.12}$$

$$\alpha(T) = \left[1 + (0.37464 + 1.5422\omega - 0.26992\omega^2)(1 - \sqrt{T/T_c})\right]^2, \tag{2.13}$$

with $a = 0.45724R^2T_c^2/p_c$ and $b = 0.0778RT_c/p_c$, where a is the attraction parameter, b is the volumetric or repulsion parameter, and ω is the acentric factor. T_c and P_c are the critical temperature and critical pressure, respectively. The density ratio and surface tension of liquid is governed by the temperature T, parameter a and b respectively. Substituting Eq. (2.12) into Eq. (2.11), we get

$$\psi(\rho) = \sqrt{\frac{2\left(\frac{\rho RT}{1-b\rho} - \frac{a\alpha(T)\rho^2}{1+2b\rho-b^2\rho^2} - c_s^2\rho\right)}{c_0 g}}. \tag{2.14}$$

Unlike in the original SC model, the value of coefficient of interaction strength g becomes unimportant. Indeed, it is canceled out when Eq. (2.11) is substituted into Eq. (2.8). The only requirement for g is to ensure that the term inside the square root in Eq. (2.11) is positive, (i.e. $g = sgn(p - c_s^2\rho)$ has to be stored when computing Eq. (2.11)).

2.3 Fluid-solid adhesion and body force

At the fluid-solid interface, the interaction between the fluid and solid interface needs to be considered, so the force applied on a particle that is in contact with the solid wall is:

$$\boldsymbol{F}_2 = -\psi(\boldsymbol{x}) \sum_{\boldsymbol{x}'} G_w(\boldsymbol{x}, \boldsymbol{x}') \rho_w(\boldsymbol{x}')(\boldsymbol{x}' - \boldsymbol{x}), \tag{2.15}$$

where $G_w(\boldsymbol{x}, \boldsymbol{x}')$ denotes the intensity of the fluid-solid interaction. For the D2Q9 model, it is defined as:

$$G_w(\boldsymbol{x}, \boldsymbol{x}') = \begin{cases} G_w g', & |\boldsymbol{x} - \boldsymbol{x}'| = 1, \\ G_w g'/4, & |\boldsymbol{x} - \boldsymbol{x}'| = \sqrt{2}, \\ 0, & \text{otherwise}, \end{cases} \tag{2.16}$$

where G_w is the fluid-solid interaction potential parameter, different contact angle can be obtained through adjusting G_w. The term $\rho_w(\boldsymbol{x}')$ in Eq. (2.15) is the wall density, which equals one at the wall and zero in the fluid. In addition to interparticle and wall forces, the body force can be simply defined as:

$$\boldsymbol{F}_3(\boldsymbol{x}) = \rho(\boldsymbol{x})\boldsymbol{g}. \tag{2.17}$$

2.4   Multi-relaxation-time LBM model

In general the collision process involves multiple physical quantities that may relax on different time scales, and information for those time scales can be given using a collision matrix Ω instead of a single time scale τ in Eq. (2.1). As a result, Eq. (2.1) is replaced by the following density distribution function:

$$
\begin{aligned}
&f_\alpha(x+e_\alpha\delta t,t+\delta t)\\
&=f_\alpha(x,t)-\sum_\beta \Omega_{\alpha\beta}[f_\beta(x,t)-f_\beta^{eq}(x,t)]+\left(S_\alpha(x,t)-0.5\sum_\beta \Omega_{\alpha\beta}S_\beta(x,t)\right),
\end{aligned}
\tag{2.18}
$$

where S is the forcing term in multi-relaxation-time LBM model which can be derived from Eq. (2.2). The collision step in the velocity space is difficult to perform. It is more convenient to perform the collision process in the momentum space. Hence, Eq. (2.18) can be transformed to the following form,

$$
f_\alpha(x+e_\alpha\delta t,t+\delta t)=f_\alpha(x,t)-M^{-1}\Lambda[m(x,t)-m^{eq}(x,t)]+M^{-1}\left(I-\frac{\Lambda}{2}\right)\bar{S}(x,t),
\tag{2.19}
$$

where m and m^{eq} are the moment space of the density distribution function f_α and its equilibrium distribution f_α^{eq} respectively. It can be obtained from $m=Mf$ and $m^{eq}=Mf^{eq}$ respectively. M is the transformation matrix, which for D2Q9 is

$$
M=\begin{bmatrix}
1 & 1 & 1 & 1 & 1 & 1 & 1 & 1 & 1\\
-4 & -1 & -1 & -1 & -1 & 2 & 2 & 2 & 2\\
4 & -2 & -2 & -2 & -2 & 1 & 1 & 1 & 1\\
0 & 1 & 0 & -1 & 0 & 1 & -1 & -1 & 1\\
0 & -2 & 0 & 2 & 0 & 1 & -1 & -1 & 1\\
0 & 0 & 1 & 0 & -1 & 1 & 1 & -1 & -1\\
0 & 0 & -2 & 0 & 2 & 1 & 1 & -1 & -1\\
0 & 1 & -1 & 1 & -1 & 0 & 0 & 0 & 0\\
0 & 0 & 0 & 0 & 0 & 1 & -1 & 1 & -1
\end{bmatrix}.
\tag{2.20}
$$

The inverse of matrix M is

$$
M^{-1}=a\begin{bmatrix}
4 & -4 & 4 & 0 & 0 & 0 & 0 & 0 & 0\\
4 & -1 & -2 & 6 & -6 & 0 & 0 & 9 & 0\\
4 & -1 & -2 & 0 & 0 & 6 & -6 & -9 & 0\\
4 & -1 & -2 & -6 & 6 & 0 & 0 & 9 & 0\\
4 & -1 & -2 & 0 & 0 & -6 & 6 & -9 & 0\\
4 & 2 & 1 & 6 & 3 & 6 & 3 & 0 & 9\\
4 & 2 & 1 & -6 & -3 & 6 & 3 & 0 & -9\\
4 & 2 & 1 & -6 & -3 & -6 & -3 & 0 & 9\\
4 & 2 & 1 & 6 & 3 & -6 & -3 & 0 & -9
\end{bmatrix},
\tag{2.21}
$$

where $a = 1/36$, I in Eq. (2.19) is the identity matrix and $\mathbf{\Lambda}$ is a diagonal matrix of multi-relaxation times which is given by

$$\mathbf{\Lambda} = diag(\tau_\rho^{-1}, \tau_e^{-1}, \tau_\zeta^{-1}, \tau_j^{-1}, \tau_q^{-1}, \tau_j^{-1}, \tau_q^{-1}, \tau_\nu^{-1}, \tau_\nu^{-1}). \tag{2.22}$$

The kinematic viscosity in the multi-relaxation-time Lattice Boltzmann model is given by

$$\nu = \left(\tau_\nu - \frac{1}{2}\right)c_s^2 \delta t. \tag{2.23}$$

The $\bar{S}$ term in Eq. (2.19) is the forcing term in the moment space which can be calculated by $\bar{S} = MS$. The force is incorporated via the following forcing scheme in the MRT LB method [34]:

$$\bar{S} = MS = \begin{bmatrix} 0 \\ 6(v_x F_x + v_y F_y) + \frac{12\epsilon F^2}{\psi^2(\tau_e - 0.5)} \\ -6(v_x F_x + v_y F_y) - \frac{12\epsilon F^2}{\psi^2(\tau_\zeta - 0.5)} \\ F_x \\ -F_x \\ F_y \\ -F_y \\ 2(v_x F_x - v_y F_y) \\ (v_x F_y + v_y F_x) \end{bmatrix}, \tag{2.24}$$

where ϵ is a constant which is given by 0.315 in current work.

3   Simulation results and discussion

3.1   Impact of a droplet onto the north pole of the tube

3.1.1   Initial and boundary condition

A two-dimensional computational domain for simulation of droplet impact onto the north pole of a tube is shown in Fig. 1. Non-slip wall boundary condition is used on the solid surface and periodic boundary condition is used on all sides of the domain. Initially, the droplet is located several nodes away from the tube and then directed towards the tube with initial velocity U_0 after 50000 lattice time steps.

3.1.2   Dynamics of the film flow on the surface of tube

Fig. 2 shows a sequence view of the impact of the droplet onto a curved target with $Re = 113.1$, $We = 12.51$, Bond number $B_0 = 1.2$, density ratio $\rho_l/\rho_g = 580$ and equilibrium contact angle $\theta = 60°$. The Bond number is defined as $B_0 = \rho_l g D_0 / \sigma$. The evolution time t is non-dimensionalized as $t^\star = t U_0 / D_0$, where D_0 is the initial drop diameter, U_0 is the initial velocity and t is the time steps elapsed after the drop contacts the surface. From this figure, the formation of the liquid lamella around the surface of the target is
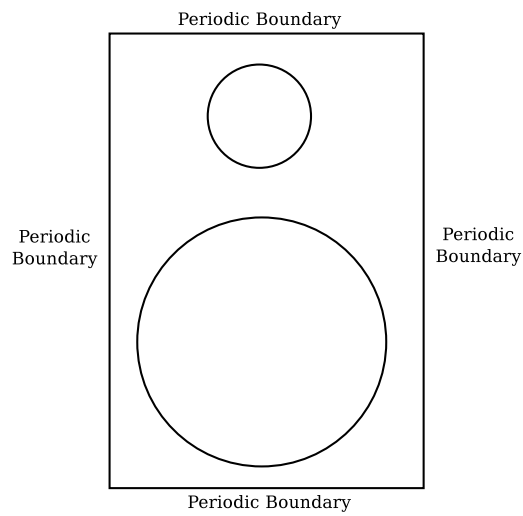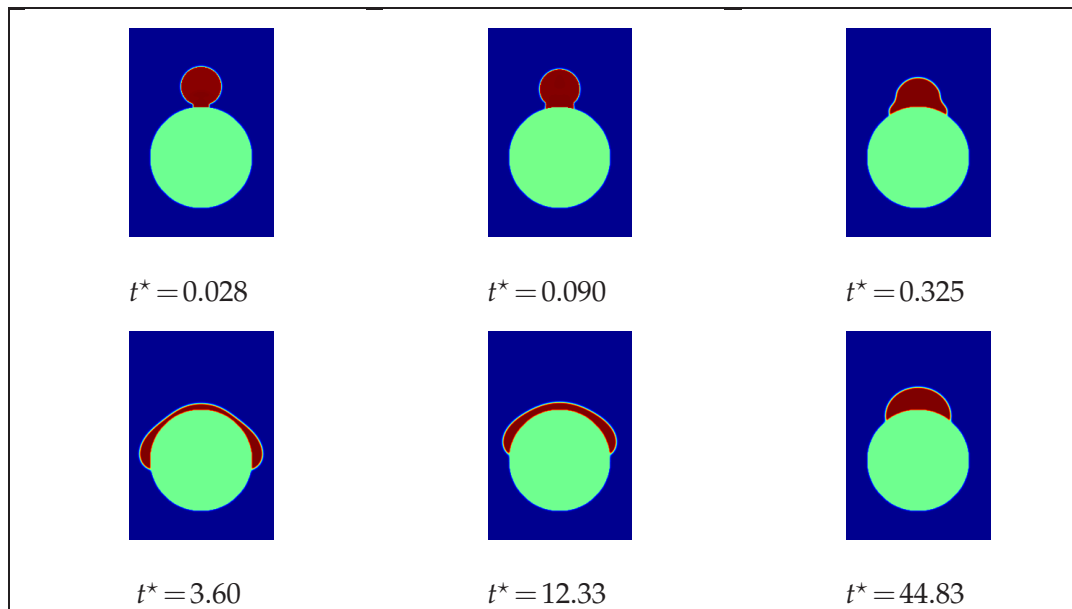
Figure 1: The initial and boundary conditions in domain.

Figure 2: Computational snapshots of droplet impact on tube; $We = 12.51$, $Re = 113.1$, density ratio= 580, contact angle= $60°$.

clearly observed. At the beginning, the initial droplet deformation period is observed. The upper portion of the droplet remains spherical under the action of surface tension and moves with the impact velocity of the drop ($t^\star = 0.028$ and $t^\star = 0.090$). Then the liquid lamella appears around the surface of the tube with the liquid continuing to flow downwards and the thickness of film at the pole of tube decreasing gradually in this
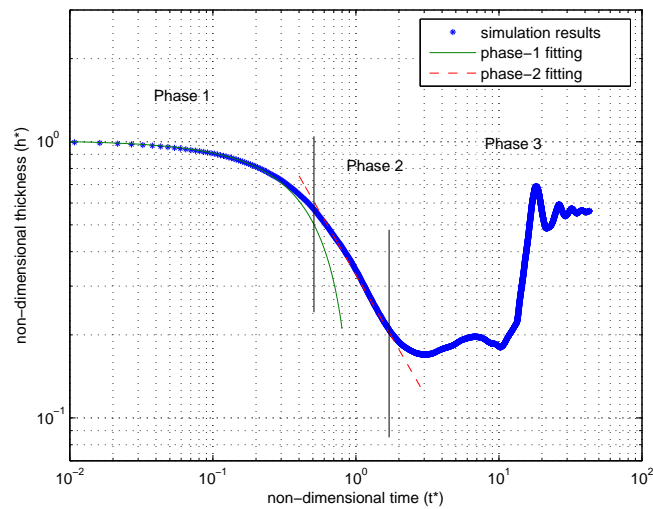
Figure 3: Time evolution of film thickness at the north pole of the tube; $We = 12.51$, $Re = 113.1$, density ratio$=580$, contact angle$=60°$.

phase ($t^\star = 0.325$ and $t^\star = 3.60$). Finally, during phase 3, the lamella begins to retract governed by the surface tension and almost reaches a residual value ($t^\star = 12.33$ and $t^\star = 44.83$) after a couple of oscillations. The corresponding temporal variation of the film thickness at the north pole of the curved target is shown in Fig. 3 with log-log axes. The film thickness is nondimensionalized with the initial impacting droplet diameter as $h^\star = h/D_0$. Three distinct temporal phases of the film dynamics can be clearly observed from this figure. The first phase is the droplet deformation period in which the free surface of the deforming drop is negligibly influenced by the presence of the target. Hence, the upper part of the droplet continues to move at the impacting velocity resulting in the non-dimensional film thickness and time satisfy the equation $h^\star = 1 - t^\star$. In the second phase, inertial forces dominate the viscous forces and surface tension, thus the temporal variation is given by the equation which yield $h^\star = 0.33/(t^\star)^{0.9}$. In phase 3, the film thickness increases under the action of surface tension and approaches a constant value due to the balance of surface tension, viscous forces and gravity.

Simulations are performed for different values of droplet Reynolds number with the same target-to-drop size ratio, wettability and kinematic viscosity to evaluate the effect of Reynolds number on the dynamics of the film flow on the surface of the tube. In order to avoid the effect of gravity, the gravity force is not included into this case. The influence of gravity on film flow dynamics will be discussed in the next paragraph. In the experimental research of Bakshi et al. [11], it has been observed that the non-dimensional temporal variation of film thickness for different values of Reynolds number collapses onto a single curve in the first and second phases. However, the Reynolds number is varied by changing the impact velocity with same kinematic viscosity value in that study. The We-

ber number is also varied during this process and both of the change of the Reynolds and Weber number affect this process. A different behaviour might be observed when only the Reynolds number is varied, while the Weber number is invariable. In order to verify this assumption, a numerical investigation is conducted as follows. Firstly, the Reynolds number is varied by changing the impact velocity, while the kinematic viscosity is kept constant. The kinematic viscosity can be controlled by Eq. (2.23) and the τ_ν is given by 0.6 for different Reynolds number. The contact angle of surface is given as $60°$ which corresponds to $G_w = 2.9$. Fig. 4 shows the time evolution of the film thickness at the north pole of the target for different Reynolds numbers. Fig. 4 shows that the non-dimensional temporal variation of film thickness for different values of Reynolds number collapses onto a single curve in the first and second phases, but the transition to the third phase occurs earlier for the low Reynolds number case. In addition, the film thickness in the third phase reduces with increasing Reynolds number. All of the above observations are in line with the experimental results by Bakshi et al. [11]. However, different phenomena can be observed for the case that different Reynolds numbers are obtained by changing the kinematic viscosity. The effect of different kinematic viscosity of fluids on the dynamics of film flow is investigated. Fig. 5 shows the time evolution of the film thickness at the north pole of the target for different Reynolds numbers through adjusting the kinematic viscosity. It can be observed that the thickness in the third phase still decreases with increasing Reynolds number. However, it does not collapse onto a single curve in the second phase for the different Reynolds number cases. The rate of film thickness decrease becomes slower with increasing kinematic viscosity. This shows that the influence of the viscous force in the second phase can not be neglected for the low Reynolds number case. By comparing with the Reynolds number and Weber number used in Bakshi et al.'s [11] experimental work, the Reynolds number and Weber number in current numerical work is low. Thus, we call the Reynolds number and Weber number in the present work as low Reynolds number and low Weber number. Actually, even for the high Reynolds number case, the influence of the viscous force will appear at the latter part of the second phase with the inertial force decreasing.

In the experimental study of Bakshi et al. [11], the effect of Reynolds number and target-to-drop size ratio on the dynamics of film flow is investigated. In the current simulation study, the influence of gravity and surface tension is investigated as well. The time evolution of the film thickness at the north pole of the tube with different Reynolds numbers at Galilei number 219.5 is shown in Fig. 6. The Galilei number is defined as $Ga = gD_0^3/\nu^2$. It is clear from Fig. 6 that the temporal variation of film thickness for different values of Reynolds number collapses onto a single curve in the first and second phases, which shows that the influence of gravity can be neglected in the first and second phases. However, decreasing the kinematic viscosity which corresponds to an increase in the Galilei number results in a different phenomenon. Fig. 7 shows the temporal variation of the film thickness for different Reynolds number at Galilei number 3512. It can be seen that the influence of gravity on the second phase appears with increasing Galilei number, while the rate of film thinning becomes slower for the high
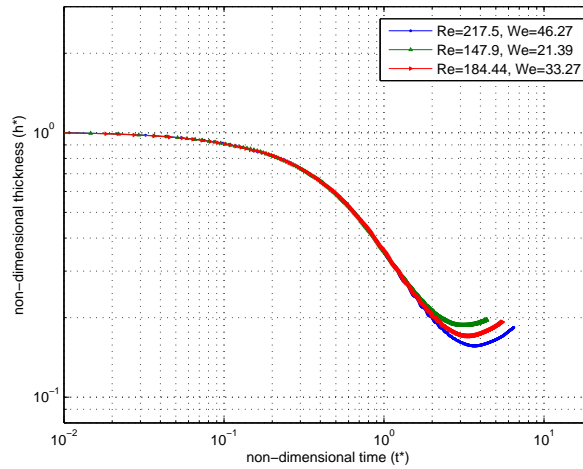
Figure 4: Temporal variation of film thickness at the north pole of the tube for different Reynolds number and Weber number with same kinematic viscosity; $\tau_\nu = 0.6$, contact angle$=60°$.
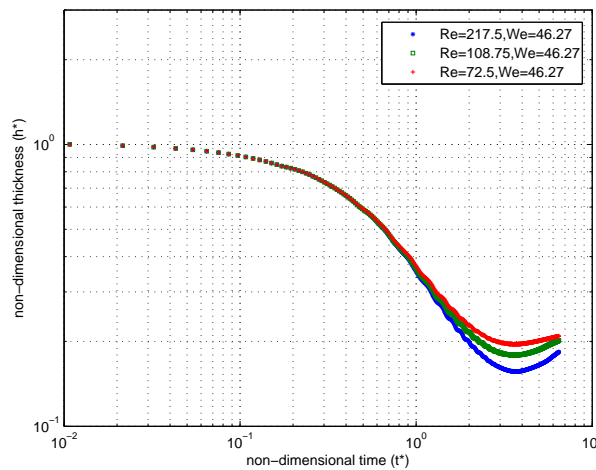

Figure 5: Temporal variation of film thickness at the north pole of the tube for different Reynolds number and Weber number with different kinematic viscosity; contact angle$=60°$.

Reynolds number case. This is because the influence of gravity is not considered into the non-dimensional time. From Fig. 8, it is clear that when evolution time t is non-dimensionalized as $t^\star = (tU_0 + 0.5gt^2)/D_0$, the non-dimensional temporal variation of film thickness for varied Reynolds number collapses onto a single curve again in the second phase. In order to evaluate the effects of the surface tension on the dynamics of the film flow process, simulations were conducted for different values of Weber number while the wettability of solid surface and Reynolds number were held constant as $\theta = 91°$
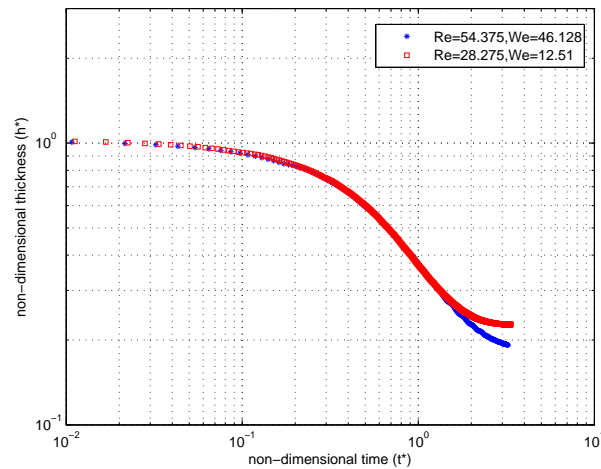
Figure 6: Temporal variation of film thickness at the north pole of the tube for different Reynolds number and Weber number with $Ga=219.5$, $B_0=3.42$, contact angle$=60°$.
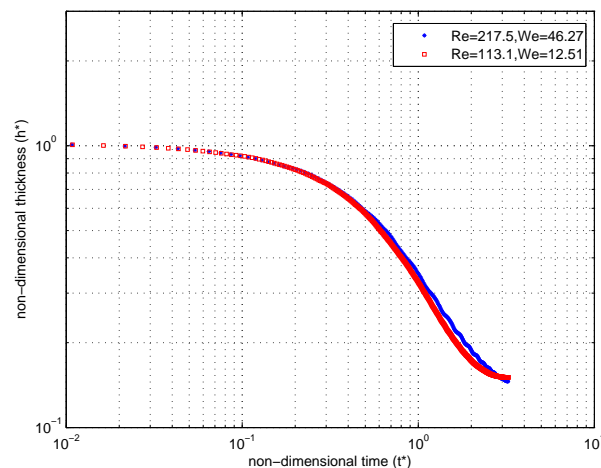

Figure 7: Temporal variation of film thickness at the north pole of the tube for different Reynolds number and Weber number with $Ga=3512$, $B_0=3.42$, contact angle$=60°$.

and 65.25. The gravity force is ignored in this case. In Fig. 9, the time evolution of the dynamics of film flow at the north pole of the tube with varied Weber number is shown. It can be seen that the effect of surface tension can be neglected in the first and second phases, and the rate of film thickness reduction is the same. However, the surface tension dominates the inertial force at the end of the second phase, the transition to the retraction phase occurs earlier for the low Weber number case.
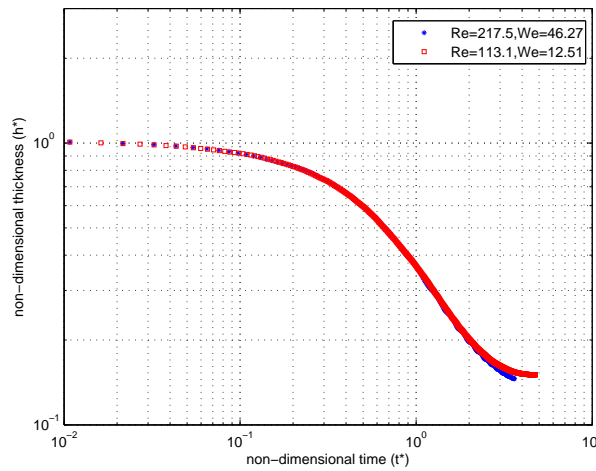
Figure 8: Temporal variation of film thickness at the north pole of the tube for different Reynolds number and Weber number with $Ga = 3512$, $B_0 = 3.42$, contact angle$= 60°$ and $t^\star = (tU_0 + 0.5gt^2)/D_0$.
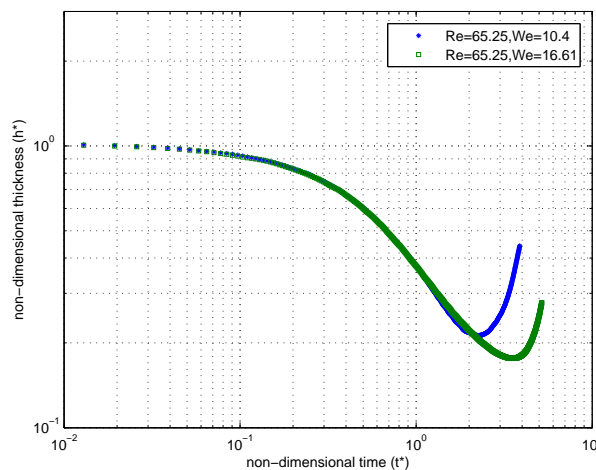

Figure 9: Temporal variation of film thickness at the north pole of the tube for different Weber number with contact angle$= 91°$ and $Re = 65.25$.

3.2   Impact of a droplet onto the side of the tube

The dynamics of the film flow at the north pole of the tube is investigated in Section 3.1.2. However, the droplet impact onto the side of the tube is a more common phenomenon in industrial equipment. Especially in fixed bed and micro-channels, the contact line between liquid and solid surface and dynamic behavior of the droplet are important for the catalytic reaction process. In the following section, the dynamic behavior of the droplet

impact onto a curved target with its center offset from the centerline of the tube is shown. The effects of the static contact angle, the Reynolds number, and the Weber number are investigated. Non-slip wall boundary conditions have been used on the sphere surface and periodic boundary conditions have been used on all sides of the domain.

3.2.1 Dynamic behavior of droplet impact onto the side of the tube

Fig. 10 shows the snapshots of impact of a liquid droplet landing on a tube, with Reynolds number of 78.3, Weber number of 23.99, Bond number of 0.515, density ratio ρ_l/ρ_g of 580 and contact angle of 107°. The droplet falls towards the tube after 50000 lattice time steps, with its center offset by 65 nodes from the centerline of the tube. The evolution time t is non-dimensionalized as $t^\star = tU_0/D_0$, where t is the number of time steps elapsed after the drop contacts the surface. Immediately after impact, the process is similar with the first phase of the droplet impact onto the north pole of the tube, which is the initial drop deformation period ($t^\star = 0.078$). Then the liquid droplet spreads out on the surface of the tube. Since the impact point of the droplet is off-set relative to the tube, the flow pattern is not symmetrical, and the majority of the liquid flows downwards rather than towards the upper part of the tube. The liquid lamella appears as the liquid flows in an upward manner towards the north pole of the tube ($t^\star = 0.62$). The upward motion tendency of the liquid is captured at $t^\star = 0.853$, where the droplet is pulled down by gravity. As a result of the inertial force and gravity, the bulk of the droplet continues to flow downwards, being stretched and growing longer and thinner ($t^\star = 1.55$ and $t^\star = 3.1$). However, with the bulk of the liquid flowing downwards, the impact and potential energy of the droplet are dissipated in overcoming the viscous flow effects and in spreading out its surface area. Hence, the downward stretching is stopped at about $t^\star = 4.19$, after which the bulk droplet is pulled back onto the tube surface under the action of surface tension force ($t^\star = 5.897$). As the downward liquid flow increases and concentrates at the bottom of the tube, the liquid droplet is stretched again under the action of the gravity and inertia ($t^\star = 8.53$). At the same time, the liquid droplet continues to move upwards along the surface of target after crossing the bottom of tube ($t^\star = 10.862$). However, the surface tension dominates the inertial and gravitational force and the upward kinetic energy is dissipated by viscous effects ($t^\star = 18.62$). Finally, the droplet flows back to the bottom under the action of gravity and continues to resemble a pendular motion until an equilibrium state is reached ($t^\star = 46.24$ and $t^\star = 62.07$).

3.2.2 Effect of contact angle

In order to investigate the effect of the wettability on the dynamic behavior of droplet after impact onto the side of tube, the droplet impacts on a hydrophilic wall (contact angle $= 75°$) and on a hydrophobic wall (contact angle $= 107°$) are simulated for the same Weber number and Reynolds number. Fig. 10 and Fig. 11 show the time evolution of droplet impact on hydrophobic and hydrophilic pipe surfaces respectively with density ratio $\rho_l/\rho_g = 580$, $Re = 78.3$ and $We = 23.99$. From Fig. 11, it can be observed that the contact line between the liquid and the solid surface is longer for the hydrophilic case than
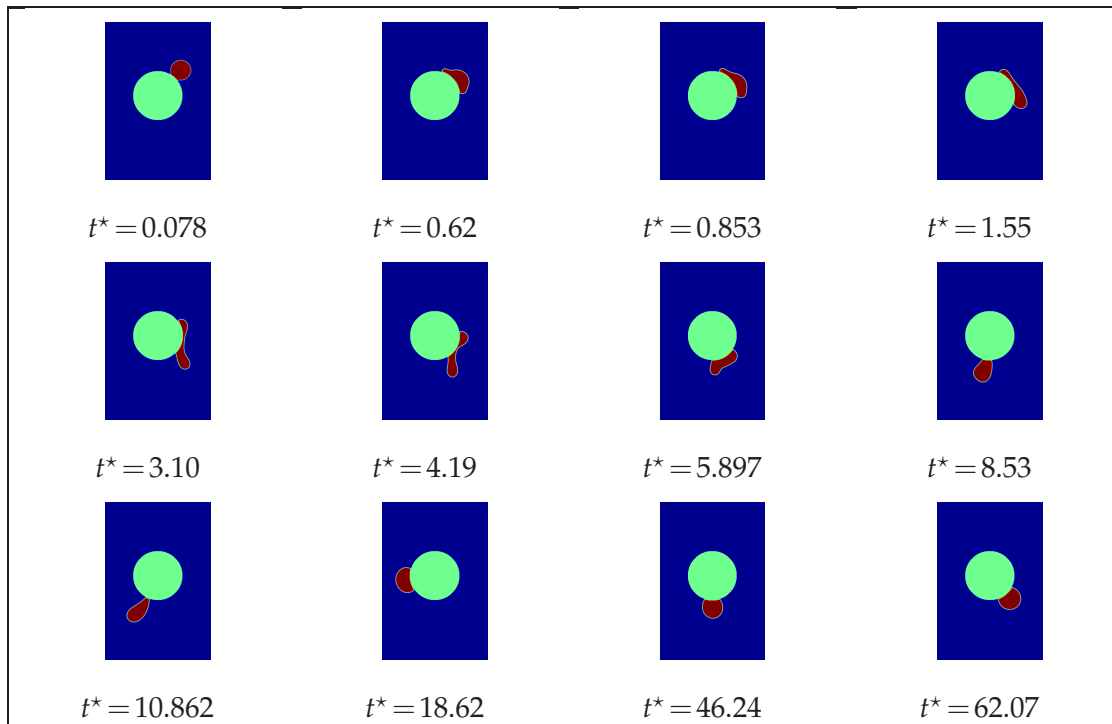
Figure 10: Computational snapshots of droplet impact on the side of tube; $We = 23.99$, $Re = 78.3$, density ratio$=580$, Bond number$=0.515$, contact angle$=107°$.

for the hydrophobic one shown in Fig. 10. In the case of hydrophilic wall, the contact line between the solid surface and the liquid is increasing with the downward liquid flow and breaks up into two parts on the surface after reaching a maximum contact line. Then the two droplets begin to retract due to interfacial tension and move towards the bottom of the tube at the same time. At $t^\star = 22.5$, the two droplets merge together, where an equilibrium shape is reached at $t^\star = 41.18$. On the other hand, in the case of the hydrophobic wall (Fig. 10), there is a process that the bulk of the droplet is stretched and grows longer and thinner as it moves along the surface of the tube. After the maximum elongation has been reached, surface tension dominates the recovery process and the droplet is attached to the tube wall. However, in the case of the hydrophilic wall (Fig. 11), the stretching and oscillation behavior is not as obvious as that in Fig. 10 and the time to reach the equilibrium state is shorter than for a hydrophobic wall. This is because of the longer contact line in the hydrophilic wall case. Thus, a higher proportion of the initial impact energy is dissipated in overcoming the viscous effects and surface tension.

3.2.3 Effect of kinetic energy

In order to investigate the dependency of the kinetic energy on the dynamic process of droplet impact onto the side of tube, simulations were conducted with various Weber
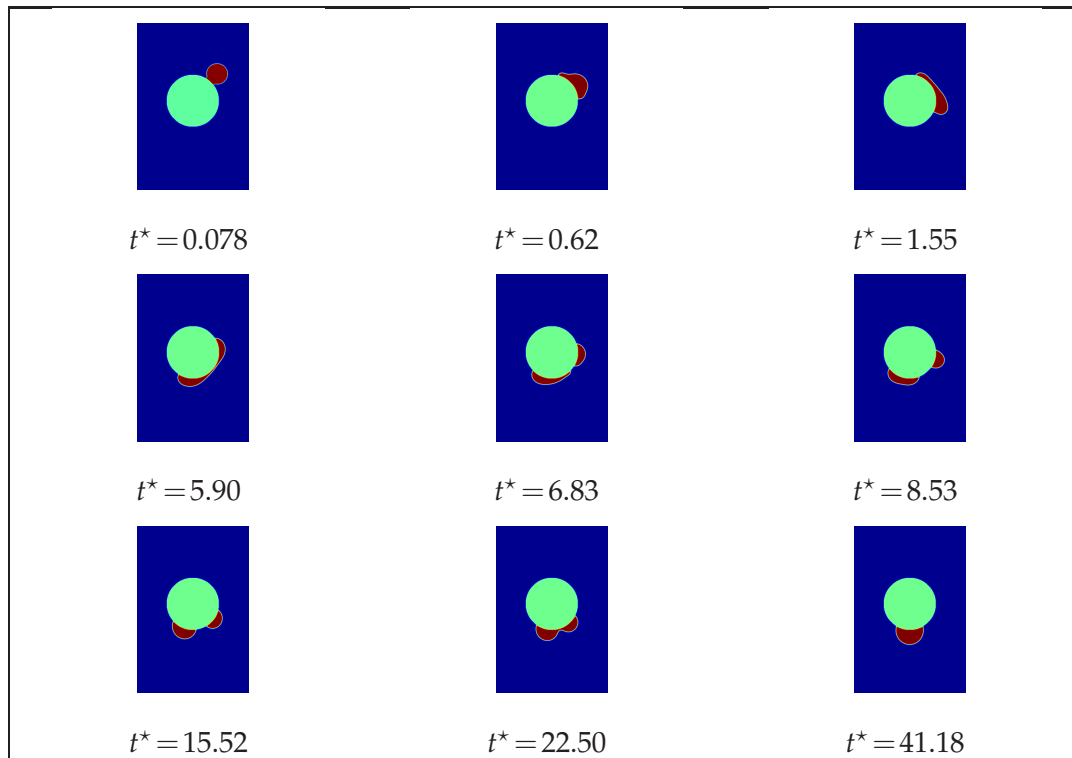
Figure 11: Computational snapshots of droplet impact on the side of tube; $We = 23.99$, $Re = 78.3$, density ratio$=580$, Bond number$=0.515$, contact angle$=75°$.

number and Reynolds numbers while the density ratio between liquid and gas, wettability of surface and Bond number were held constant.

Fig. 12 shows the time simulated images of the dynamic behavior of the liquid droplet impact onto the side of the tube with Weber number 46.27 and Reynolds number 108.75. The values of contact angle and Bond number are the same as in Fig. 10. It can be seen from Fig. 12, that the liquid breaks up into three smaller drops on the surface with the film thinning and contact area increasing. The third part of the drop continues to flow downwards with higher velocity and results in a column of liquid being suspended from the tube ($t^* = 5.17$). The velocity of the lower portion of the droplet is larger than that in the upper portion, which causes the lower portion of the bulk of the liquid to be pinched off from the upper portion. Then the upper portion is subsequently detached from the tube due to inertia dominating surface tension ($t^* = 6.42$ and $t^* = 7.25$). Thus, as it is expected, higher Weber number flows will result in surface droplet breakup and droplet detachment from the tube, something that does not occur in lower Weber number flows (Fig. 10). In addition, since the surface is non-wetting, the liquid has a reduced affinity for the solid surface, and in turn the surface interactions from the solid reduce the surface energy. This leads to the less initial kinetic energy of droplet be dissipated and a strong
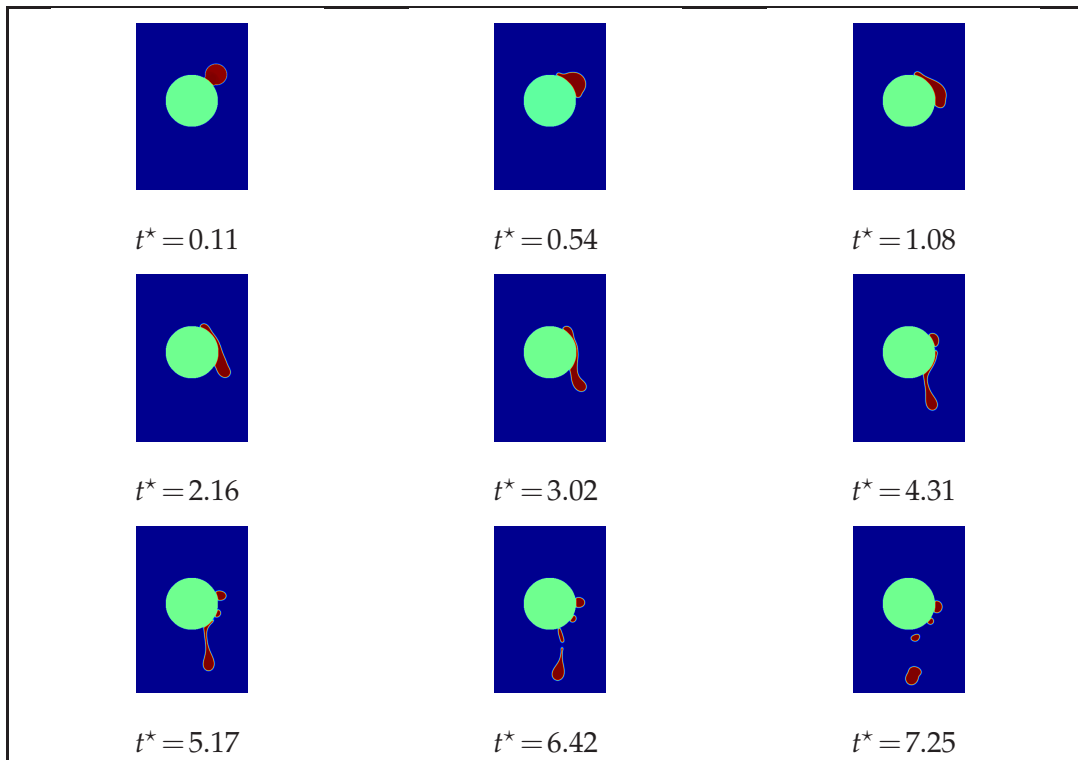
Figure 12: Computational snapshots of droplet impact on the side of tube; $We = 46.27$, $Re = 108.75$, density ratio$=580$, Bond number$=0.515$, contact angle$=107°$.

liquid elongation flow along the surface eventually leads to a breakup of the droplet on the surface. In order to validate the above conclusion, a case of hydrophilic surface wall (contact angle $= 60°$) which has the same Weber number and Reynolds number as in Fig. 12 is performed. From Fig. 13, it can be observed that the surface droplet breakup does not occur in hydrophilic surface due to the higher kinetic energy dissipation on surface energy. However, similar to the hydrophobic case shown in Fig. 12, the bulk of the droplet suspends below the tube and detachment occurs as the liquid elongation reaches a critical state at $t^\star = 6.79$.

4 Conclusions

In the present work, the liquid droplet impact on a curved target has been simulated by a two-dimensional multi-relaxation time (MRT) lattice Boltzmann model which can tolerate high density ratios and low viscosity. It is shown that three distinct temporal phases of the film dynamics can be clearly observed from the simulation results which is consistent with the experimental study of Bakshi et al. [11]. In the first phase, the non-dimensional film thickness follows the correlation given by $h^\star = 1 - t^\star$. The inertia dominates the vis-
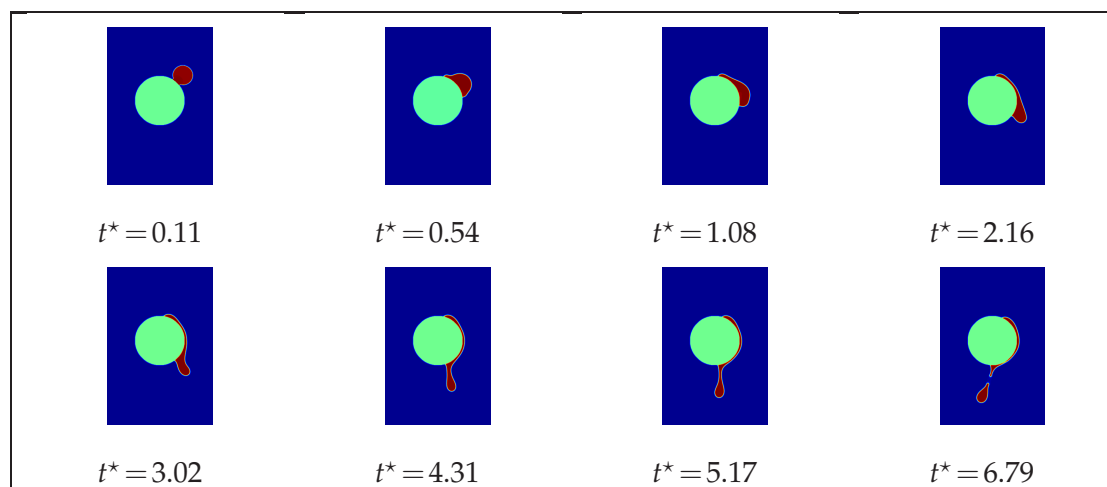
Figure 13: Computational snapshots of droplet impact on the side of tube; $We = 46.27$, $Re = 108.75$, density ratio$=580$, Bond number$=0.515$, contact angle$=60°$.

cous forces during the second phase, while the non-dimensional time and film thickness satisfy the relation $h^* = 0.33/(t^*)^{0.9}$. In the third phase, the film thickness increases under the action of the interfacial tension and almost reaches a constant value at last due to the balance of surface tension, viscous force and gravity. The non-dimensional time and film thickness curve for different values of Reynolds number collapses onto a single curve in the first and second phases which is in line with the experimental results [11] when the Reynolds number is controlled by the impact velocity. However, different phenomena can be observed for the case that varied Reynolds number obtained by changing the kinematic viscosity. It can be seen that the non-dimensional time and film thickness curves for varied Reynolds number do not collapse onto a single curve in the second phase, and the rate of film thickness reduction becomes slower with increasing kinematic viscosity. Therefore, the influence of the viscous force in the second phase can not be neglected for the low Reynolds number case. The effects of gravity and surface tension on the dynamics of film flow are also investigated in the current paper. It is found that the influence of gravity on the second phase appears with increasing Galilei number, the rate of film thinning becomes slower for the high Reynolds number case when evolution time is non-dimensionalized as $t^* = tU_0/D_0$, while the film thickness reduction rate will remain the same when $t^* = (tU_0 + 0.5gt^2)/D_0$. From the simulation results, the effect of surface tension can be neglected at the first and second phases, while the surface tension dominates the inertial force at the end of the second phase, the transition to the retraction phase occurs earlier for low Weber numbers.

The investigation of dynamic behavior of droplet impact on the side of the tube is also included in this study. At the same time, the effects of surface characteristics and impact velocity on the dynamic behavior are evaluated. From the simulation study, it can be concluded that the contact line between liquid and solid surface on hydrophilic

wall is longer than for hydrophobic surface and higher kinetic energy will be dissipated on the hydrophilic wall. In addition, increasing the initial kinetic energy will result in a droplet breakup and in the case of high impact velocity, the use of a hydrophilic surface can assist in averting the surface droplet breakup during the impacting process.

Acknowledgments

References

[1] M. Rein, Phenomena of liquid drop impact on solid and liquid surface, Fluid Dyn. Res., 38(1993), 61.
[2] A. L. Yarin, Drop impact dynamics: Splashing, spreading, receding, bouncing···, Annu. Rev. Fluid Mech., 38(2006), 159-192.
[3] R. Rioboo, M. Marengo and C. Tropea, Time evolution of liquid drop impact onto solid, dry surfaces, Exp. Fluids, 33(2002), 112-124.
[4] A. Asai, M. Shioya, S. Hirasawa and T. Okazaki, Impact of an ink drop on paper, J. Imaging Sci. Techn., 37(1993), 205-207.
[5] B. L. Scheller and D. W. Bousfield, Newtonian drop impact with a solid surface, AIChE J., 41(1995), 1357-1367.
[6] M. Pasandideh-Fard, Y. M. Qiao, S. Chandra and J. Mostaghimi, Capillary effects during droplet impact on a solid surface, Phys. Fluids, 8(1996), 650.
[7] T. Mao, D. C. S. Kuhn and H. Tran, Spread and rebound of liquid droplets upon impact on flat surfaces, AIChE J., 43(1997), 2169-2179.
[8] I. V. Roisman, R. Rioboo and C. Tropea, Normal impact of a liquid drop on a dry surface: Model for spreading and receding, Proc. R. Soc. London, Ser. A 458(2002), 1411-1430.
[9] L. S. Hung and S. C. Yao, Experimental investigation of the impaction of water droplets on cylindrical objects, Int. J. Multiphase Flow, 25(1999), 1545-1559.
[10] Y. Hardalupas, A. M. K. P. Taylor and J. H. Wilkins, Experimental investigation of submillimeter droplet impingement onto spherical surfaces, Int. J. Heat Fluid Flow, 20(1999), 477-485.
[11] S. Bakshi, L. V. Roisman and C. Tropea, Investigations on the impact of a drop onto a small spherical target, Phys. Fluids, 19(2007), 032102.
[12] G. Trapaga and J. Szekely, Mathematical modeling of the isothermal impingement of liquid droplets in spraying processes, Metall. Trans. B, 22(1991), 901-914.
[13] M. Bussmann and S. Afkhami, Drop impact simulation with a velocity-dependent contact angle, Chem. Eng. Sci., 62(2007), 7214.
[14] M. Pasandideh-Fard, M. Bussmann, S. Chandra and J. Mostaghimi, Simulating droplet impact on a substrate of arbitrary shape, Atomization Spray., 11(2001), 397-414.
[15] H. Liu, S. Krishnan, S. Marella and H. S. Udaykumar, Sharp interface Cartesian grid method II: A technique for simulating droplet interactions with surfaces of arbitrary shape, J. Comput. Phys., 210(2005), 32-54.

[16] Y. Ge and L. S. Fan, Droplet-particle collision mechanics with film-boiling evaporation, J. Fluid Mech., 573(2007), 331-337.

[17] X. Shan and H. Chen, Simulation of nonideal gases and liquid-gas phase transitions by the lattice Boltzmann equation, Phys. Rev. E, 49(1994), 2941-2948.

[18] M. R. Swift, E. Orlandini, W. R. Osborn and J. M. Yeomans, Lattice Boltzmann simulations of liquid-gas and binary fluid systems, Phys. Rev. E, 54(1996), 5041-5052.

[19] X. He, S. Chen and R. Zhang, A lattice Boltzmann scheme for incompressible multi-phase flow and its application in simulation of Rayleigh-Taylor instability, J. Comput. Phys., 152(1999), 642-663.

[20] T. Inamuro, T. Ogata, S. Tajima and N. Konishi, A lattice Boltzmann method for incompressible two-phase flows with large density differences, J. Comput. Phys., 198(2004), 628-644.

[21] Y. Y. Yan and Y. Q. Zu, A lattice Boltzmann method for incompressible two-phase flows on partial wetting surface with large density ratio, J. Comput. Phys., 227(2007), 763-775.

[22] A. J. Briant, P. Papatzacos and J. M. Yeomans, Lattice Boltzmann simulations of contact line motion in a liquid-gas system, Philos. Trans. Roy. Soc. Lond. A, 360(2002), 485-495.

[23] T. Lee and L. Lin, Lattice Boltzmann simulations of micron-scale drop impact on dry surfaces, J. Comput. Phys., 229(2010), 8045-8063.

[24] G. Kaehler and A. J. Wagner, Derivation of hydrodynamics for multi-relaxation time lattice Boltzmann using the moment approach, Commun. Comput. Phys., 13(2013), 614-628.

[25] L. Wang, Z. L. Guo, B. C. Shi and C. G. Zheng, Evaluation of three lattice Boltzmann models for particulate flows, Commun. Comput. Phys., 13(2013), 1151-1172.

[26] Q. X. Li, N. Hong, B. C. Shi and Z. H. Chai, Simulation of power-law fluid flows in two-dimensional square cavity using multi-relaxation-time lattice Boltzmann method, Commun. Comput. Phys., 15(2014), 265-284.

[27] A. Gupta and R. Kumar, Droplet impingement and breakup on a dry surface, Comput. Fluids, 39(2010), 1696-1703.

[28] A. Gupta and R. Kumar, Two-dimensional lattice Boltzmann model for droplet impingement and breakup in low density ratio liquids, Commun. Comput. Phys., 10(2011), 767-784.

[29] S. Q. Shen, F. F. Bi and Y. L. Guo, Simulation of droplets impact on curved surfaces with lattice Boltzmann method, Int. J. Heat Mass Tranf., 55(2012), 69386943.

[30] Q. Li, K. H. Luo and X. J. Li, Forcing scheme in pseudopotential lattice Boltzmann model multiphase flows, Phys. Rev. E, 86(2012), 016709.

[31] P. Yuan and L. Schaefer, Equations of state in a lattice Boltzmann model, Phys. Fluids, 18(2006), 042101.

[32] Z. Guo, C. Z and B. Shi, Discrete lattice effects on the forcing term in the lattice Boltzmann method, Phys. Rev. E, 65(2002), 046308.

[33] Z. Yu and L. S. Fan, Multirelaxation-time interaction-potential-based lattice Boltzmann model for two-phase flow, Phys. Rev. E, 82(2010), 046708.

[34] Q. Li, K. H. Luo and X. J. Li, Lattice Boltzmann modeling of multiphase flows at large density ratio with an improved pseudopotential model, Phys. Rev. E, 87(2013), 053301.